Chapter 6

Robust Damping Control Scheme for VSG-Enabled Inverter-Based Resources at Low Inertia Bus in Power Networks to Mitigate Low-Frequency Oscillations

6.1 Introduction

This chapter presents the impact of multiple Inverter-Based Resources(IBRs) controlled through the Virtual Synchronous Generator (VSG) on power system Low-Frequency Oscillations (LFOs). IBRs are integrated into the low-inertia bus, identified using the Geometric Measurement of Observability (GMO) index for the prominent LFO mode of the system. The dynamic interaction between the power network and active and reactive power loops of IBR with varying parameters such as inertia constant (H), damping coefficient (D_p), and voltage gain coefficient (k_q) influences the system LFO damping. Further, the Supplementary Damping Control (SDC) scheme for IBRs is proposed to enhance system LFO damping and mitigate the power oscillations of IBRs. This SDC consists of a multi-stage mixed H_2/H_∞ decentralized damping controller linked with the IBR's active control loop and the Power System Stabilizer (PSS) linked with the reac-

tive control loop of the IBR, whose parameters are tuned using the loop tune method. The robustness of the proposed SDC is validated on the New England 39-bus system under various system operating conditions, such as load increments, changes in network topology, and integration of renewable sources. Eigenvalue analysis is conducted using MATLAB, while dynamic simulations are performed using the Real-Time Digital Simulator (RTDS). Simulation results confirm that the proposed SDC effectively mitigates system LFO and power oscillations in IBRs.

6.2 System Modelling

This study investigates the damping impact on power system LFOs by integrating IBRs controlled through VSG techniques. Appropriate modelling of all power system components is essential for conducting eigenvalue analysis. In this work, each SG is represented by a 6th-order model equipped with an IEEE type I excitation system and a type I governor system. PSSs are also employed to control SG locally. The transmission line is modelled as a π model, and loads are modelled as constant impedance type load models. The subsequent subsection discusses the topology and mathematical modelling of IBRs controlled through the VSG technique.

6.2.1 VSG topology and principle

The IBRs controlled through the VSG control technique are depicted in Fig. 6.1. The power part consists of the DC source represented by V_{dc} and IBR (i.e. 3-phase two-level Voltage Source Converter (VSC)) connected to the power network through the filter and coupling transformer, where R_V, L_V, and C_V are the equivalent resistance, inductance, and capacitance of the filter, respectively. Among these components, I_c, V_s, and I_s are the current flow in filter inductance, voltage across filter capacitance, and output current (i.e. current at the Point of Common Connection (PCC)), respectively. The control part of the VSG technique consists of an outer control loop, which includes an Active Power Controller (APC) and a Reactive Power Controller (RPC), respectively. Furthermore, the inner control loop of VSG consists of the voltage control loop, current limitation control, and current control loop, respectively.

The primary objective of the APC loop of the VSG technique is to generate a ref-

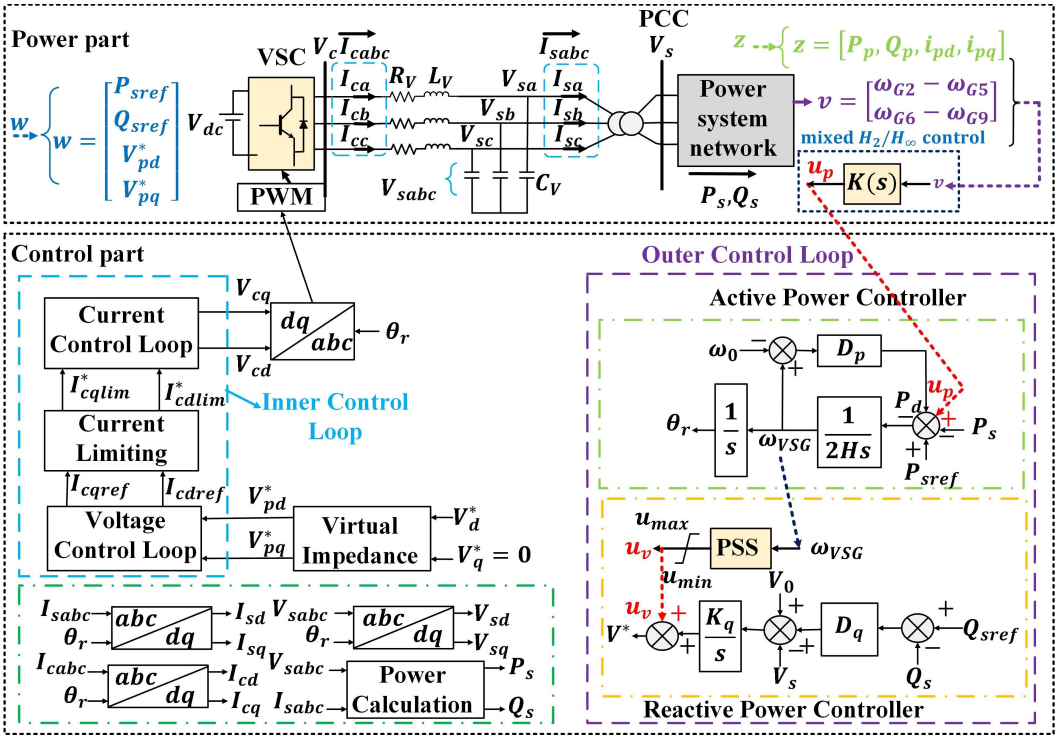

Figure 6.1: VSG topology and associated supplementary control scheme.

erence angle θ_r to synchronize IBR to the power network based on the swing equation of an SG. The active control loop of the VSG technique includes a virtual governor and a virtual rotor, respectively. Meanwhile, the reactive control loop of the VSG employs an integral controller to generate the voltage magnitude V^*, which is referred to as a virtual Automatic Voltage Regulator (AVR). The output signal V^* from the reactive control is linked with a virtual winding to generate reference signals V^*_{pd} and V^*_{pq} for the voltage control loop. Subsequently, the voltage control loop is connected with the current limiting control and control loop to produce control signals V_{cd} and V_{cq} for pulse width modulation, thereby controlling the VSC and regulating the PCC voltage V_s.

The rotor motion equation of the APC loop of IBR controlled through the VSG technique, as depicted in Fig. 6.1, is expressed as:

$$\begin{cases} 2H\dfrac{d\omega_{VSG}}{dt} = P_s - P_{sref} - D_p\left(\omega_{VSG} - \omega_0\right) \\ \dfrac{d\theta_r}{dt} = \omega_{VSG} - \omega_0 \end{cases} \tag{6.1}$$

where, D_p and H are the virtual damping coefficient and virtual inertia constant, respectively; P_s and P_{sref} are the IBR output active power and active power reference, respectively; ω_{VSG} and ω_0 are the VSG angular frequency and grid angular frequency; θ_r

is the virtual rotor angle.

The voltage regulation of IBR controlled through the VSG technique is emulated by the virtual AVR using droop control, as depicted in Fig. 6.1, which can be expressed as :

$$V^* = K_q \int \left[D_q \left(Q_{sref} - Q_s \right) + \left(V_0 - V_s \right) \right] dt \tag{6.2}$$

where, Q_{sref} and Q_s are the IBR reactive power and reactive power reference, respectively; D_q is the droop coefficient of the Q–V, and $P-\omega$ loop; K_q, and V^* are the reactive power adjustment coefficient, and output voltage of the virtual excitation loop.

6.2.2 Inner loop control design of VSG

The inner control loop of the VSG technique is linked with virtual impedance (i.e., virtual winding) from the outer reactive power control loop, as depicted in Fig. 6.1. The inner control loop of the VSG technique is shown in Fig. 6.2. The subsequent sub-section presents a comprehensive discussion of the detailed modelling of the virtual winding, voltage control loop, and current control loop employed in the VSG control technique in this work.

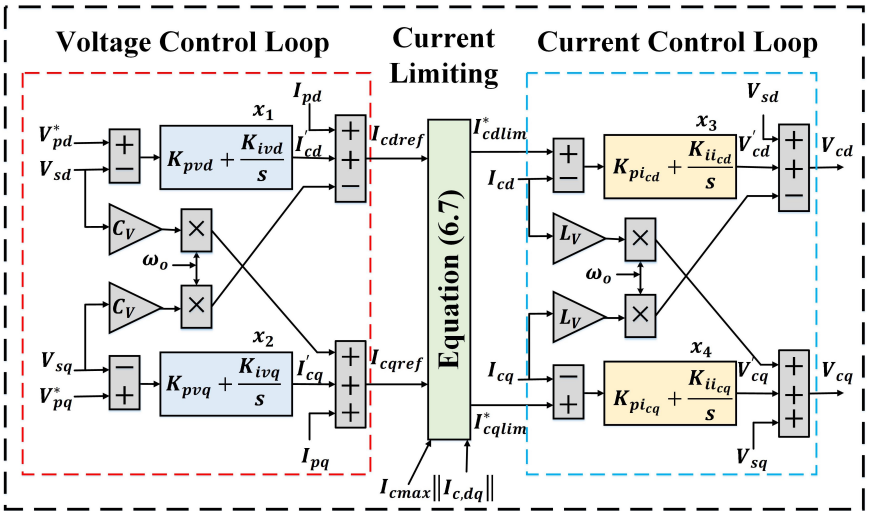

Figure 6.2: Inner control loop of IBR control via VSG technique.

6.2.2.1 Modelling of virtual winding

The virtual winding in the VSG technique mimics the synchronous machine's electromagnetic characteristics. The virtual winding of VSG linked to the voltage control loop is

expressed as:

$$\begin{cases} V_{pd}^{*} = V_{d}^{*} - R_v I_{sd} + X_v I_{sd} \\ V_{pq}^{*} = V_{q}^{*} - R_v I_{sq} - X_v I_{sq} \end{cases} \tag{6.3}$$

where, R_v and X_v are the virtual resistance and virtual reactance, respectively; $V_d^*, V_q^*, V_{pd}^*, V_{pq}^*, I_{sd}$, and I_{sq} are the out voltage of the virtual AVR, reference voltage generated for the voltage control loop, and current at the PCC are in the dq reference frame, respectively

6.2.2.2 Modelling of voltage control loop

The dynamic equation describing the voltage across the filter capacitor in the dq reference frame is expressed as follows:

$$\begin{cases} C_V \dfrac{dV_{pd}}{dt} = I_{cd} + I_{sd} + \omega C_V V_{sq} \\ C_V \dfrac{dV_{pq}}{dt} = I_{cq} + I_{sq} - \omega C_V V_{sd} \end{cases} \tag{6.4}$$

The integral control of the voltage control loop, as shown in Fig. 6.2, is described with state variables x_1 and x_2 in the dq reference frame, respectively, and is expressed as:

$$\begin{cases} \dfrac{dx_1}{dt} = K_{ivd}\left(V_{pd}^{*} - V_{sd}\right) \\ \dfrac{dx_2}{dt} = K_{ivq}\left(V_{pq}^{*} - V_{sq}\right) \end{cases} \tag{6.5}$$

where, K_{ivd} and K_{ivq} are the integral gain coefficient of the voltage control loop of VSG control in the dq reference frame, respectively.

The reference current generated for the current limiting control in the dq-reference frame can be expressed as follows:

$$\begin{cases} I_{cdref} = I_{sd} + I_{cd}^{'} - \omega C_V V_{sq} \\ I_{cqref} = i_{sq} + I_{cq}^{'} + \omega C_V V_{sd} \end{cases} \tag{6.6}$$

where, $I_{cd}^{'} = K_{pvd}\left(V_{pq}^{*} - V_{sq}\right) + x_1$, and $I_{cq}^{'} = K_{pvq}\left(V_{pq}^{*} - V_{sq}\right) + x_2$; K_{pvd}, and K_{pvq} are the proportional gain coefficient of voltage control loop in the dq-refrance frame, respectively.

6.2.2.3 Current limiting control

The VSG control technique employs the current limiting control scheme to prevent the converter current from exceeding safe operating limits during abnormal conditions, as shown in Fig. 6.2. The current limiting scheme is expressed in dq-reference frame as follows [27]:

$$I^*_{clim,dq} = \begin{cases} I^*_{c,dq}, if \|I_{cref,dq}\| \leq I_{cmax} \\ \gamma_i I_{cref,dq}, if \|I_{c,dq}\| \geq I_{cmax} \end{cases} \tag{6.7}$$

where,$\gamma_i = \left(\dfrac{I_{cmax}}{\|I_{cref,dq}\|}\right)$.

6.2.2.4 Modelling of current control loop

The dynamic equation of the VSC output current flow through filter reactance in the dq reference frame is expressed using (4.2) of chapter-4.

The integral control of the current control loop, as depicted in Fig. 6.2, is defined with state variables x_3 and x_4 in the dq reference frame, respectively and is expressed as:

$$\begin{cases} \dfrac{dx_3}{dt} = K_{ii_{cd}} \left(I^*_{cdlim} - I_{cd}\right) \\ \dfrac{dx_4}{dt} = K_{ii_{cq}} \left(I^*_{cqlim} - I_{cq}\right) \end{cases} \tag{6.8}$$

where, $I^*_{cdlim}, I^*_{cqlim}, K_{ii_{cd}}$ and $K_{ii_{cq}}$ are the reference current generation, and integral gain coefficient of integral control of the current control loop in the dq-axis, respectively.

The reference output voltage generated for the VSC in the dq-reference frame may be expressed as:

$$\begin{cases} V_{cd} = V_{sd} + V^{'}_{cd} - \omega L_V I_{cq} \\ V_{cq} = V_{sq} + V^{'}_{cq} + \omega L_V I_{cd} \end{cases} \tag{6.9}$$

where, $V^{'}_{cd} = K_{pi_{cd}} \left(I^*_{cdlim} - I_{cd}\right) + x_3$, and $V^{'}_{cq} = K_{pi_{cq}} \left(I^*_{cqlim} - I_{cq}\right) + x_4$; $K_{pi_{cd}}$, and $K_{pi_{cq}}$ are the proportional gain coefficient of current control loop in the dq-refrance frame, respectively.

The state-space model for IBRs controlled through the VSG control technique in the dq reference frame is formulated using (6.1) to (6.9) and is presented as follows:

$$\begin{cases} \dot{x}_{VSG} = A_{VSG} x_{VSG} + B_{VSG} u_{VSG} \\ y_{VSG} = C_{VSG} x_{VSG} + D_{VSG} u_{VSG} \end{cases} \tag{6.10}$$

where, $x_{VSG} = [\omega, \theta_r, V^*, V_{sd}, V_{sq}, x_1, x_2, I_{cd}, I_{cq}, x_3, x_4]^T$, $u_{VSG} = [V_{sq}, P_{sref}, Q_{sref}]^T$, and $y_{VSG} = [P_s, Q_s]^T$ are the state vector, input vector, and output vector, respectively, for the state model of IBR controlled through the VSG technique. The matrices $A_{VSG}, B_{VSG}, C_{VSG}$, and D_{VSG} correspond to the system, input, output, and feed-forward coefficients.

6.2.3 Power system model

The power system model in this study comprises the SGs nonlinear model,*pi* model of transmission lines, constant impedance type loads, and IBRs with associated VSG control techniques described in previous sub-sections, respectively. The set of differential and algebraic equations describes this model. The state-space model of the power system is described using (3.8) of chapter-3.

6.3 Damping Analysis of the System with IBRs Controlled via the VSG Technique

This section investigates how multiple IBRs controlled through the VSG technique, including the variation of VSG parameters, such as H and D_p, affect power system LFO modes damping. Additionally, this study examines how the dynamic interaction between the VSG control loop and the rest of the power system affects LFO damping and system stability, as well as how the state variables of VSG control influence the system's prominent LFO.

6.3.1 Study system description

This work utilizes the New England 39-bus benchmark system as a study test system, shown in Fig. 6.3, to assess the impact of system LFO damping with integrating multiple IBRs.The details of the study system are given in Appendix-C. The entire system is divided into three areas by the inter-area tie lines connecting bus-39 to bus-1 (Area-1 to Area-3), bus-14 to bus-15 (Area-1 to Area-2), and bus-17 to bus-27 (Area-2 to Area-3). The Area-1, Area-2, and Area-3 are placed with generators SG1-SG3, SG4-SG7, and SG8-SG10, respectively. Further, SG2, SG4, SG8, and SG10 excitation systems incorporate

PSS, and the gain of PSSs is 50 times higher than specified in [92]. The study system parameters are taken from [92].

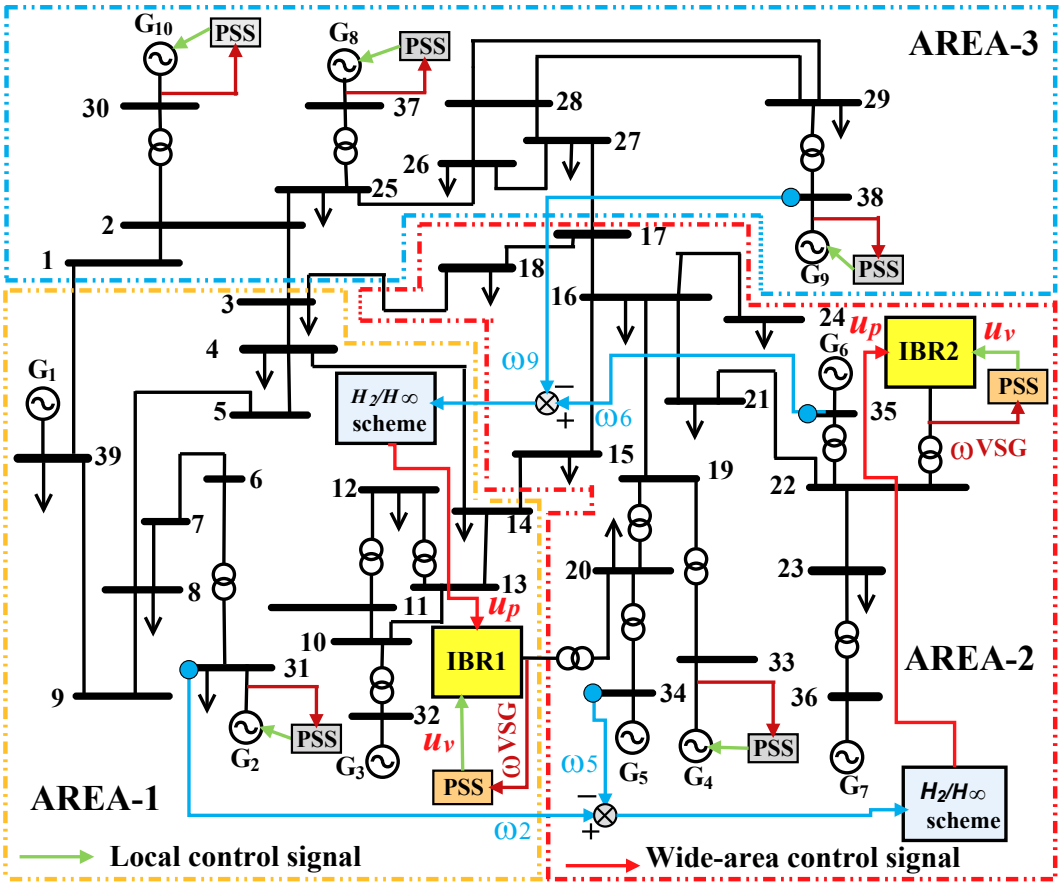

Figure 6.3: A New England 39-bus system with IBRs controlled via VSG technique.

6.3.2 Impact on system damping performance for IBRs controlled through VSG technique and grid-following technique

The primary objective is to assess the impact of integrating IBRs on system LFO mode damping. This work identifies suitable locations for IBR placement to enhance damping performance. Furthermore, it presents a comparative analysis of damping effects on system LFO modes without IBRs and with IBRs controlled using grid-following (i.e., $P-Q$ control) and VSG techniques.

6.3.2.1 Damping performance of study system without IBR

The damping performance of the study system's LFO modes without integrating IBR is shown in Table 6.1. In this system, certain oscillation modes exhibit poor damping characteristics. Specifically, two local oscillation modes ($\lambda_{1,2}$ and $\lambda_{3,4}$) and two inter-area oscillation modes ($\lambda_{5,6}$ and $\lambda_{7,8}$) are observed, as present in Table 6.1. Among these, the oscillation mode $\lambda_{7,8}$ stands out with a damping ratio of less than 5% and an oscillation frequency below 1Hz, indicating significant inter-area oscillation of system instability. In this mode, SG G4 swings against SGs G9, G10, G1, and G2 (i.e., Area 2 vs. Area 3 and Area 1).

Table 6.1: Study system LFO modes without IBR

Mode	**Eigenvalue and damping ratio**	**Modes shape**
$\lambda_{1,2}$	$-0.4986 \pm i9.3605$ $(\xi = 5.32\%\ ,\ f = 1.489Hz)$	G_4 vsG_5, G_6, G_7 Area-2 (Local mode)
$\lambda_{3,4}$	$-0.6037 \pm i9.0832$ $(\xi = 6.63\%\ ,\ f = 1.445Hz)$	G_8 vs G_9, G_{10} Area-3 (Local mode)
$\lambda_{5,6}$	$-0.2986 \pm i5.1341$ $(\xi = 5.81\%\ ,\ f = 0.817Hz)$	G_4, G_5, G_6, G_7, vs $G_8 G_9, G_{10}$ Area 2 vs Area3 (Inter-area mode)
$\lambda_{7,8}$	$-0.1038 \pm i3.8396$ $(\xi = 2.70\%\ ,\ f = 0.611Hz)$	G_4, vs (G_9, G_{10}) & (G_1, G_2) Area 2 vs Area3 & Area 1 (Inter-area mode)

6.3.2.2 Appropriate location of IBR in the power network

This work uses the Geometric Measurement of Observability (GMO) index based on eigenvalue analysis to find the appropriate location to integrate the IBRs in the power system. The GMO ($gm_{oj}(k)$) associated with mode k is calculated using (2.24) of chapter-2.

The GMO indices for the load bus voltage angle of the study system in inter-area oscillation modes $\lambda_{5,6}$ and $\lambda_{7,8}$ are shown in Fig. 6.4. From this result, it can be observed that the GMO index for buses 20 and 22 is the maximum, while buses 1 and 9 have the minimum GMO index. Additionally, it is observed that the GMO index of other buses are lower compared to buses 20 and 22 in the system's inter-area modes, $\lambda_{5,6}$ and $\lambda_{7,8}$. The bus with the maximum observability in the system's inter-area modes typically represents

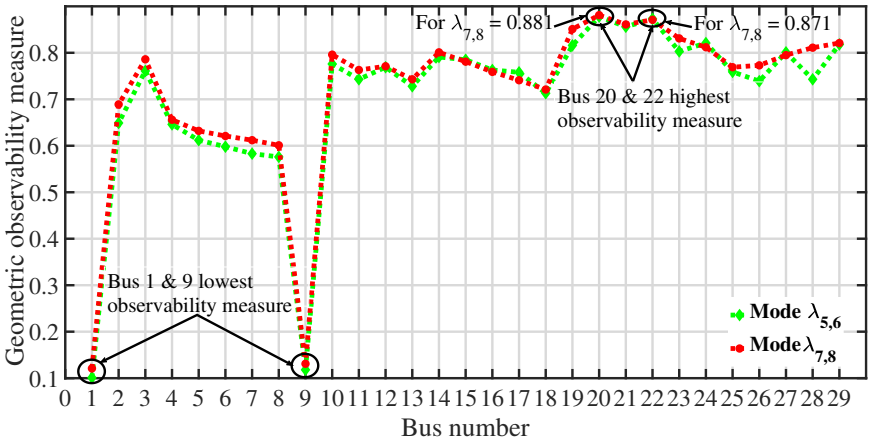

Figure 6.4: Geometric observability measure of the load buses of study system in prominent LFO modes.

the low inertia bus, which is associated with the system's maximum oscillatory response. Therefore, to enhance damping performance in the prominent oscillation mode, IBRs are strategically placed at the low inertia bus of the system. Consequently, buses 20 and 22 are identified as appropriate locations for integrating IBRs(i.e., IBR1 and IBR2) into the system, as shown in Fig. 6.3.

6.3.2.3 Damping performance of study system with IBRs

In this work, the VSC of IBRs is modelled as an aggregate model with a specified power capacity of 250 MW. The damping performance and SG rotor speed mode shape for LFO modes of study system with IBRs controlled through $P-Q$ technique are shown in Table 6.2.

Table 6.2: Study system LFO modes with IBRs controlled via $P-Q$ control technique

Mode	**Eigenvalue and damping ratio**	**Modes shape**
$\lambda_{1,2}$	$-0.5422 \pm i8.8961$ ($\xi = 6.09\%$, $f = 1.415Hz$)	G_4 vsG_5, G_6, G_7 Area-2 (Local mode)
$\lambda_{3,4}$	$-0.6243 \pm i8.6377$ ($\xi = 7.21\%$, $f = 1.374Hz$)	G_8 vs G_9, G_{10} Area-3 (Local mode)
$\lambda_{5,6}$	$-0.3011 \pm i4.8766$ ($\xi = 6.16\%$, $f = 0.77Hz$)	G_4, G_5, G_6, G_7, vs $G_8 G_9, G_{10}$ Area 2 vs Area3 (Inter-area mode)
$\lambda_{7,8}$	$-0.1225 \pm i3.2509$ ($\xi = 3.77\%$, $f = 0.51Hz$)	G_4, vs (G_9, G_{10}) & (G_1, G_2) Area 2 vs Area3 & Area 1 (Inter-area mode)

The damping performance of system LFO modes with IBRs control through the $P-Q$ control technique is slightly improved compared to the system without integration of IBRs, as shown in Tables 6.1 and 6.2, while the rotor speed mode shape of each LFO mode is the same. Generally, IBRs controlled via the $P-Q$ technique have fast dynamics but offer minimal additional damping support for power system LFOs [102]. These IBRs lack inertia and damping characteristics, essentially behaving as static elements. Consequently, integrating IBRs with the $P-Q$ control technique does not introduce new LFO modes to the system.

The LFO damping performance of the system integrated with IBRs controlled through the VSG technique and the corresponding rotor speed-based mode shape of each oscillation mode are presented in Table 6.3. From these results, it is observed that the damping performance and oscillation characteristic (i.e., mode shape of rotor speed) of system LFO oscillation modes without and with the integration of IBRs controlled through the VSG technique has improved and changed, respectively. The IBRs controlled with the VSG technique have altered the oscillation characteristic of inter-area mode $\lambda_{7,8}$ of the system without IBRs. In systems without IBRs, this mode involves the rotor swinging of SG $G4$ against SGs $G9, G10, G1, G2$, as shown in Table 6.1. However, with IBRs controlled by VSG, the mode shape of this mode has changed, which involves the rotor swinging of SGs $G2, G3$ against SGs $G4, G5, G6, G7, VSG2$, as shown in Table 6.3.

Table 6.3: Study system LFO modes with IBRs controlled via VSG technique

Mode	**Eigenvalue and damping ratio**	**Modes shape**
$\lambda_{1,2}$	$-0.5573 \pm i8.9476$ ($\xi = 6.23\%$, $f = 1.424Hz$)	G_4 vsG_5, G_6, G_7 Area-2 (Local mode)
$\lambda_{3,4}$	$-0.6451 \pm i8.4592$ ($\xi = 7.60\%$, $f = 1.346Hz$)	G_8 vs G_9, G_{10} Area-3 (Local mode)
$\lambda_{5,6}$	$-0.2976 \pm i4.8432$ ($\xi = 6.14\%$, $f = 0.770Hz$)	G_4, G_5, G_6, G_7, vs $G_8 G_9, G_{10}$ Area 2 vs Area3 (Inter-area mode)
$\lambda_{7,8}$	$-0.1275 \pm i3.2691$ ($\xi = 3.90\%$, $f = 0.520Hz$)	G_2, G_3, vs $G_4, G_5, G_6, G_7, VSG2$ Area 1 vs Area 2 (Inter-area mode)
$\lambda_{9,10}$	$-0.5373 \pm i7.9476$ ($\xi = 6.78\%$, $f = 1.264Hz$)	G_5, G_6, G_7, vs $VSG1, VSG2$ Area 2 (Local mode)
$\lambda_{11,12}$	$-0.2361 \pm i4.1836$ ($\xi = 5.63\%$, $f = 0.665Hz$)	$G_5, G_6, G_7, VSG1$, vs (G_9, G_{10}) Area 2 vs Area3 (Inter-area mode)

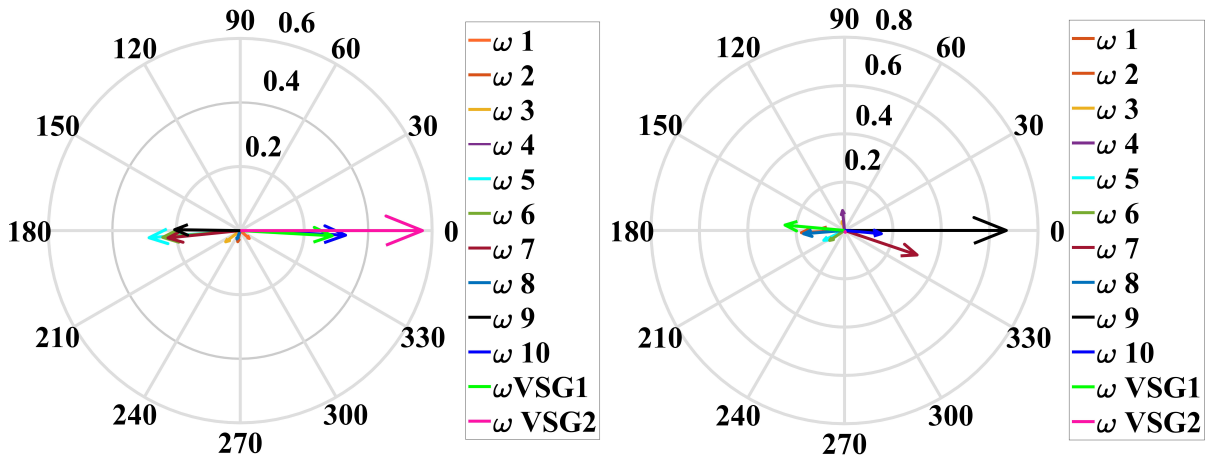

(a) (b)

Figure 6.5: Rotor speed mode shape for new LFO mode introduced by IBRs control via VSG technique in New England 39-bus system. (a) Mode $\lambda_{9,10}$, and (b) Mode $\lambda_{11,12}$.

Further, from this analysis, it is found that the IBRs with the VSG control technique introduced the new local and inter-area oscillation modes $\lambda_{9,10}$ and $\lambda_{11,12}$, respectively. The oscillation mode $\lambda_{9,10}$ of SGs $G5, G6, G7$ is swinging against the rotor speed of $VSG1, VSG2$, as shown in Fig. 6.5 (a). Similarly, oscillation mode $\lambda_{11,12}$ of SGs and VSG1 $G5, G6, G7, VSG1$ is swinging against the rotor speed of SGs $G9, G10$, as shown in Fig. 6.5(b).

6.4 Impact of dynamic interaction between IBRs and power networks on system LFO modes

This section investigates how the dynamic interaction between the VSG control loop and the rest of the power system affects LFO damping and system stability, as well as how the state variables of VSG control influence the system's prominent LFO.

6.4.1 Interaction between active power loop of IBRs and power network

The active power control loop of IBR1 and IBR2 varies its virtual inertia constant (H) from $42s$ to $50s$ with a step of 2 to analyze the effect on system dynamic behaviour in LFO modes. The virtual damping constant (D_p) of the IBR1 and IBR2 active power

control loop is held constant at 60 p.u. The corresponding eigenvalue plot and damping performance are shown in Fig. 6.6 (a) and (b), respectively.

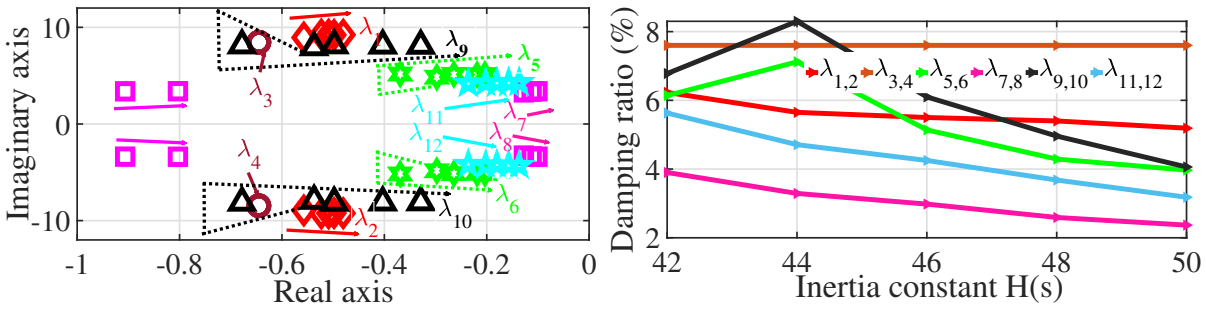

(a) (b)

Figure 6.6: Study system with the change of the H of IBRs associated with the VSG technique. (a) Eigenvalue plot, and (b) Damping ratio plot.

Fig. 6.6 shows that with an increase in the virtual inertia constant of IBRs, oscillation modes $\lambda_{7,8}, \lambda_{11,12}$, and $\lambda_{1,2}$ shift towards the right in the complex plane. Consequently, the damping ratio of these modes decreases from 3.90% to 2.368%, 5.63% to 3.18%, and 6.23% to 5.19%, respectively. On the other hand, oscillation modes $\lambda_{9,10}$ and $\lambda_{5,6}$ initially shift leftwards and then move to the right plane, resulting in an initial increase followed by a decrease in damping performance. Notably, oscillation mode $\lambda_{3,4}$ exhibits no significant movement, leading to no changes in damping performance. Further, the influence of virtual inertia on oscillation mode $\lambda_{1,2}$ is significantly smaller compared to modes $\lambda_{7,8}, \lambda_{9,10}$, and $\lambda_{11,12}$.

From this analysis, it is observed that in the oscillation modes of the system involving IBRs, higher values of virtual inertia lead to a reduction in damping performance and an increase in the frequency of these modes. However, this effect is more pronounced in inter-area oscillations compared to local-area oscillations in the same area.

Moreover, each IBR varies its virtual damping constant from 60 p.u. to 80 p.u. with a step of 5, while the virtual inertia constant of each IBR is 42 s. As observed in Fig. 6.7, oscillation modes $\lambda_{7,8}, \lambda_{11,12}$, and $\lambda_{1,2}$ shift to the left plane, with their damping ratios increasing from less than 3.9% to over 8%. However, oscillation mode $\lambda_{3,4}$ exhibits no significant movement, leading to no changes in damping performance. Further, oscillation modes $\lambda_{5,6}$ and $\lambda_{1,2}$ show significant improvements in damping ratio, as shown in Fig. 6.7(b).

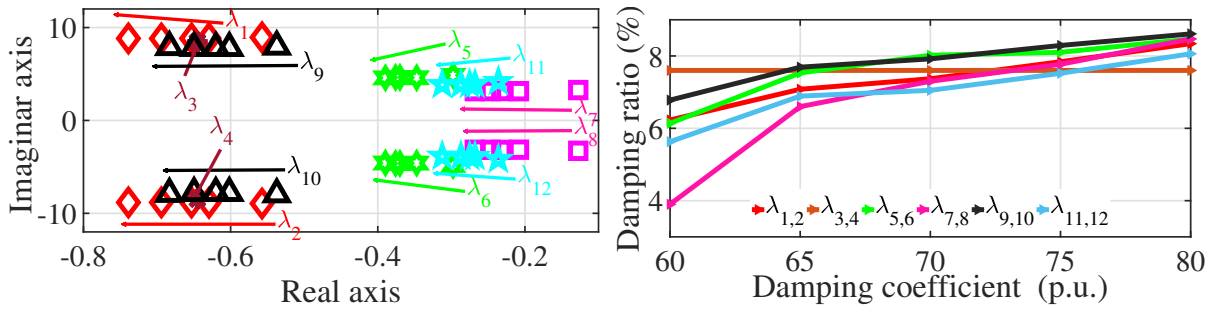

(a) (b)

Figure 6.7: Study system with the change of the D_p of IBRs associated with the VSG technique. (a) Eigenvalue plot, and (b) Damping ratio plot.

The increase in the virtual damping constant notably enhances the damping ratio of LFO modes involving IBRs, while reducing their oscillation frequency.

6.4.1.1 Interaction between reactive power loop of IBRs and power network

The voltage gain coefficient k_q of each IBR is increased from 0.05 p.u to 0.25 p.u with the step of 0.05 to analyse the impact of system LFO damping due to control mode interaction between the reactive power loop of IBRs and the power network.

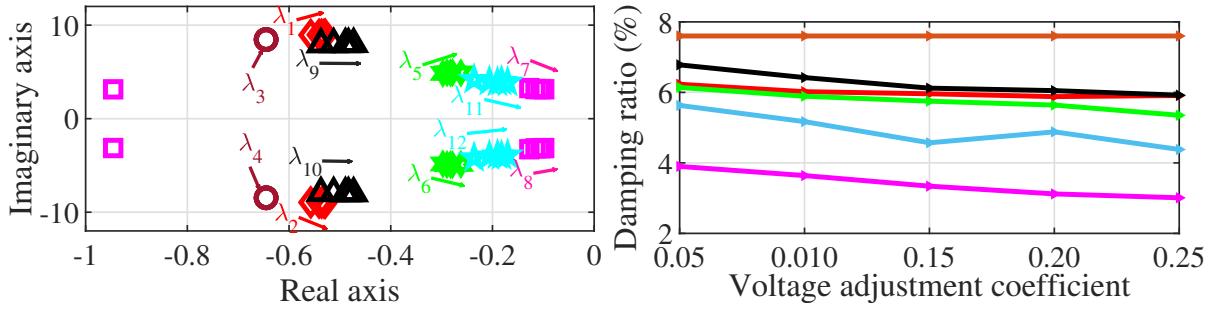

(a) (b)

Figure 6.8: Study system with the change in k_q of IBRs controlled through the VSG technique. (a) Eigenvalue plot, and (b) Damping ratio plot.

This analysis shows that as the value of k_q increases, the system's LFO modes slightly shift towards the right side of the complex plane, as illustrated in Fig. 6.8(a). Simultaneously, there is a reduction in system oscillation damping, as depicted in Fig. 6.8(b), and an increase in the frequency of oscillation of LFO modes, except for oscillation mode $\lambda_{3,4}$. Consequently, the system's LFO damping experiences a marginal decrease with the increase of the voltage gain coefficient in the reactive control loop of IBRs, thereby di-

minishing system stability. Furthermore, the dynamic interaction between IBRs and the power network's control modes affects the oscillation damping of LFOs.

6.4.2 Contribution of IBRs state variables in system LFO modes

The description of the state variable of IBRs with the VSG control technique is presented in Section 6.2. The contribution of the state variables of IBR1 and IBR2 with virtual inertia constants of $42s$ and $50s$ on system LFO modes are shown in Fig. 6.9. Additionally, participation factor analysis identifies the contribution of IBRs' state variables in LFO modes $\lambda_{7,8}$, $\lambda_{9,10}$, and $\lambda_{11,12}$, which include IBRs.

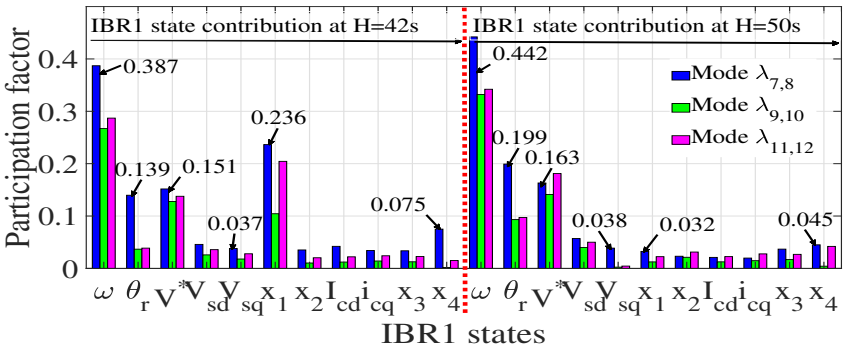

(a)

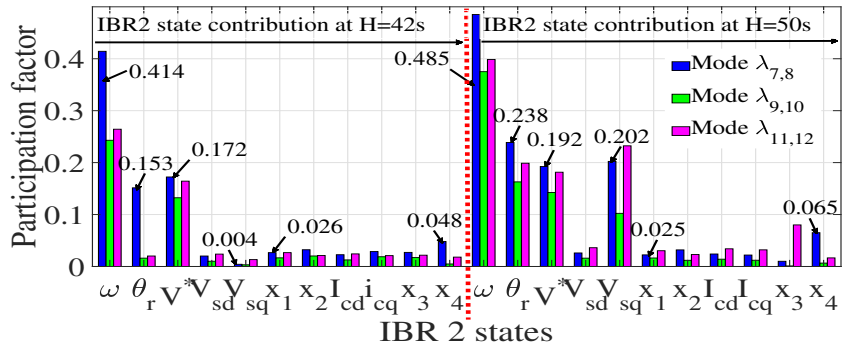

(b)

Figure 6.9: Participation of IBR state variables with virtual inertia constants of $42s$ and $50s$ in system LFO modes: (a) IBR 1, and (b) IBR 2.

From Fig. 6.9, it is evident that in system oscillation mode $\lambda_{7,8}$, the contribution of state variables ω, θ_r, and V^* is obtained as 0.485 p.u., 0.238 p.u., and 0.192 p.u., respectively, for IBR 2 with a virtual inertia constant of the $50s$, which is higher compared to IBR 2 with a virtual inertia constant of $42s$ and IBR 1 with virtual inertia constants of $50s$ and $42s$.

On the other hand, in oscillation mode $\lambda_{7,8}$, the remaining state variables, excluding ω, θ_r, V^*, and V_{sq}, for IBR 1 with a virtual inertia constant of $42s$ exhibit higher contributions compared to IBR 1 with a virtual inertia constant of $50s$ and IBR 2 with virtual inertia constants of both $42s$ and $50s$. Thus, ω, θ_r, and V^* emerge as the dominant state variables of IBRs with increased virtual inertia constants, significantly impacting the damping performance of system LFO modes $\lambda_{7,8}$, $\lambda_{9,10}$, and $\lambda_{11,12}$. Further, the remaining state variables, excluding ω, θ_r, and V^*, do not have a significant impact on IBRs with an increased virtual inertia constant. As a result, these state variables do not make substantial contributions to system LFO modes $\lambda_{7,8}$, $\lambda_{9,10}$, and $\lambda_{11,12}$

The virtual inertia constant of IBRs significantly influences the contribution of state variables to system LFO modes, affecting system stability.

6.5 Supplementary Damping Control Scheme for IBRs

In Section 6.4, it was discussed that increasing the virtual inertia constant in the active control of IBRs and the voltage gain coefficient in the reactive control loop of IBRs led to a reduction in system damping performance in LFO modes. Therefore, this work proposed an SDC scheme for IBRs shown in Fig. 6.1 to mitigate system LFOs and improve system stability. This SDC consists of the mixed H_2/H_∞ control scheme for the active control loop of IBRs and the PSS for the reactive control loop of IBRs.

6.5.1 Designing a multi-stage mixed H_2/H_∞ scheme-based decentralized damping controller for IBRs

The primary aim of multi-stage mixed H_2/H_∞ scheme-based output feedback control is to enhance the power system's robustness against model uncertainty and external disturbances. Various factors, such as the integration of wind power sources, power network line outages, fluctuations in load, and parametric variations in the IBR control loop, are considered uncertainties in this study. Parametric uncertainty in the IBR control loop is modelled through a multiplicative perturbation approach, as recommended in [103]. Furthermore, the H_2 control method enhances the system's transient response, focusing on minimizing control effort, while H_∞ control ensures system stability against uncertainties. Damping requirements are met by imposing constraints on the placement of closed-loop

poles during control design.

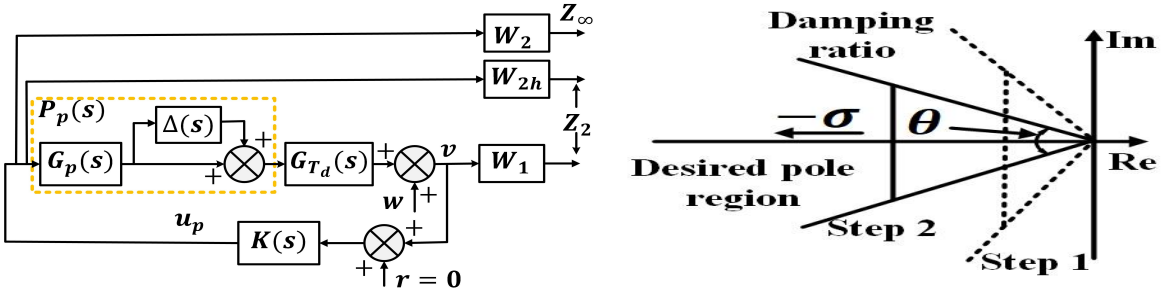

(a) (b)

Figure 6.10: Damping controller structure: (a) Configuration of mixed H_2/H_∞ scheme, and (b) Multi-stage pole placement region.

The configuration of the multi-objective H_2/H_∞ damping control scheme is shown in Fig. 6.10(a). $P_p(s)$ is the power system model that includes the parameters perturbation of the proportional gain coefficient of the voltage control loop of IBRs. The $G_p(s)$ represents the power system model without the IBRs control loop perturbations. $K(s), u, \Delta(s), G_{T_d}(s), w$, and v are the transfer functions model, the output signal, perturbation block, time delay model, external input, and measured output of the damping controller, respectively. Further, the wide-area signal is used as the feedback signal to design the damping controller, so it becomes imperative to factor in transmission time delay T_d during the control design phase. Consequently, this work employs the second-order time delay model using the Pade approximation associated with the damping controller, which is expressed as follows:

$$G_{T_d}(s) = \frac{T_d^2 s^2 - 6T_d s + 12}{T_d^2 s^2 + 6T_d s + 12} \tag{6.11}$$

In the damping controller structure shown in Fig. 6.10(a), the Z_2 and Z_∞ are the output channels that are linked to the H_2 and H_∞ performances, respectively. The low pass filter $W_1(s)$ is linked to the H_2 performance channel to reject output disturbances, and the small constant or high pass filter $W_{2h}(s)$ is linked to the H_2 performance channel to reduce the control effort of damping controller. The H_∞ performance channel is linked to the high pass filter $W_2(s)$ to ensure robustness against system uncertainties. Moreover, the impact of a disturbance can be obtained using the sensitivity transfer function from the disturbance input w to the measured output v:

$$S(s) = (I - P_p(s)\, G_{T_d}(s)\, K(s))^{-1} \tag{6.12}$$

The transfer matrix from w to Z_2 for H_2 channel is expressed as:

$$M_{wz_2} = \begin{bmatrix} W_1(s)S(s) \\ \\ W_{2h}(s)K(s)S(s) \end{bmatrix} \tag{6.13}$$

The performance objective of the damping controller, which includes control effort minimization and rejection of output disturbances, is achieved by minimizing the H_2 norm $\|M_{wz_2}(s)\|_2$. Additionally, the transfer matrix from w to Z_∞ for H_∞ channel is expressed as :

$$M_{wZ_\infty} = W_2(s)K(s)S(s) \tag{6.14}$$

In the presence of uncertainty in the power system, the closed-loop system can increase its robustness and stability by decreasing the H_∞ norm $\|M_{wz_\infty}\|_\infty$.

Further, to address the multi-objective control problem shown in Fig. 6.10(a), a pole placement constraint is incorporated into the damping controller's design phase to improve the closed-loop system's transient response. The pole of the system's predominant oscillation mode is intentionally shifted to the left side of the complex plane, referred to as the Linear Matrix Inequality (LMI) region, as shown in Fig. 6.10(b). This adjustment ensures the desired damping performance of the system's LFOs.

The multi-objective mixed H_2/H_∞ control scheme for the active control loop of IBR at each stage is formulated as follows:

$$\begin{aligned} \min_{K(s)} \quad & A_\infty \|M_{wz_\infty}(s)\|_\infty^2 + A_2 \|M_{wz_2}(s)\|_2^2 \\ \text{s.t.} \quad & \text{Poles} \in D_r \end{aligned} \tag{6.15}$$

where A_∞ and A_2 are the weight of the H_∞ and H_2 performance channel.

6.5.2 Design of supplementary damping control scheme for IBRs

6.5.2.1 Multi-stage mixed H_2/H_∞ scheme-based damping controller designed for IBRs

The multi-stage mixed H_2/H_∞ control design scheme is presented in Section 6.5.1. This damping control approach is designed for the active power control loop of each IBRs (i.e, IBR1 and IBR2) in the study system. Parametric uncertainty is introduced into the power system model by adjusting the proportional gain coefficients (K_{pvd} and K_{pvq}) of the voltage control loop's dq reference frame for each IBRs. The range of parametric variation uncertainty is $\pm 20\%$ with a step of 0.05. This uncertainty is incorporated into the design process of the damping controller.

The order of the study system with IBRs linearized model under normal operating conditions is obtained as 146. To simplify the design process, the Schur model order reduction technique [44] is used to reduce the system complexity. The study system is reduced to an 8^{th}-order system model, preserving the LFO mode of interest for the damping controller design.

The rotor speed of the most dominant SG in the system's LFO is chosen as the wide-area feedback signal for the damping controller, as shown in Table 6.3. Specifically, the rotor speed difference between SG6 and SG9 is used as the wide-area feedback signal for designing the damping controller for IBR1, while the rotor speed difference between SG2 and SG5 is selected for IBR2. These wide-area signals are measured using PMUs placed on G2, G5, G6, and G9 buses of the study test system. A communication time delay of 150 ms is considered in the feedback loop during the damping controller's design process. Furthermore, disturbance inputs ($P_{sref}, Q_{sref}, V_{pd}$, and V_{pq}) and regulated outputs (P_s, Q_s, I_{sd}, and I_{sq}) are considered during the damping controller's design stage.

The transfer function of the weight shaping filter, as shown in Fig. 6.10(a), is selected as:

$$W_1(s) = \frac{25}{s+25}, W_{2h}(s) = 0.3, W_2(s) = \frac{12s}{s+80} \tag{6.16}$$

The control problem described in (6.15) regarding the mixed H_2/H_∞ control for the active control loop of the IBRs is solved using the MATLAB function *hinfmix*. Weight parameters A_∞ and A_2 are set to 0.6 to achieve the desired performance objectives for the damping controller, including the required damping performance and robustness against

system uncertainties. This work sequentially synthesizes a mixed H_2/H_∞ scheme-based WADC for IBR1 and IBR2 in two stages. In the first stage, a damping controller is designed for IBR1, targeting a desired damping ratio of 10% and settling time of $10s$. Accordingly, $\theta_1 = 168.52^\circ$ and $\sigma_1 = 0.4$ are chosen for pole placement region. Similarly, in the second stage, a damping controller is designed for IBR2, with a desired damping ratio of 12% and settling time of $8s$, selecting $\theta_2 = 166.21^\circ$ and $\sigma_2 = 0.5$ for the pole placement region.

The WADC designed for IBR1 and IBR2 initially has a high order of 10^{th} (comprising an 8^{th}-order reduced order system and a 2^{nd}-order weight shaping filter), which may pose practical challenges. The Schur model reduction technique reduces the 10^{th}-order WADC-designed model to the 5^{th}-order model. The transfer function models of the designed WADC for IBR1 and IBR2, obtained using (6.15) , are expressed as:

$$T_{IBR1}(s) = \frac{N_{IBR1}}{D_{IBR1}} \tag{6.17}$$

where, $N_{IBR1} = 0.107s^4 - 206s^3 + 1625s^2 + 2.136 \times 10^4 s + 0.02 \times 10^5$

$D_{IBR1} = s^5 - 1919s^4 + 2.73 \times 10^4 s^3 + 1.623 \times 10^4 s^2 + 1.067 \times 10^4 s + 1.013 \times 10^5$

$$T_{IBR2}(s) = \frac{N_{IBR2}}{D_{IBR2}} \tag{6.18}$$

where, $N_{IBR2} = 2.921s^4 - 1.97 \times 10^4 s^3 + 7.336 \times 10^4 s^2 + 3.317 \times 10^5 s + 0.361 \times 10^6$

$D_{IBR2} = s^5 - 7485s^4 + 9660s^3 + 3.936 \times 10^5 s^2 + 4.072 \times 10^5 s + 1.018 \times 10^5$

6.5.2.2 Design of PSS for reactive control loop of IBR

In this work, PSS is designed using the loop tune technique and links with the reactive power control loop of IBR control through the VSG technique. The input signal of PSS is taken as the rotor speed of VSG (i.e., local signal), and the output signal of PSS is linked to the reactive control loop of IBR. The control structure of PSS is expressed in (2.5) of chapter-2.

The parameters of the PSS are tuned using the *systune* function available in MATLAB. The output signal of the PSS is constrained within the range of [-0.10, 0.10]. The control structure of the PSS for each IBR reactive control is expressed as follows:

$$T_{PSS}(s) = \frac{7.93s^3 + 14.49s^2 + 8.07s + 1.27}{s^3 + 20.28s^2 + 4.98s + 0.051} \tag{6.19}$$

6.6 SDC Performance Validation and Dynamic Simulation Analysis

6.6.1 Robustness validation of proposed SDC for IBRs

The design of the SDC scheme for IBRs is presented in Section 6.5.2. This work validates the robustness of the damping performance of the proposed SDC scheme for IBRs in the system LFO mode against various system operating uncertainties, as discussed in Table 6.4.

Table 6.4: Study system operating uncertainty

Operating condition 1	The study system operates under normal conditions.
Operating condition 2	Switch off the inter-area transmission line between buses 2–3; Integrate the 250 MW power rating of WTS at bus 1; Increase the load active power at buses 25, 26, 27, and 29 by 10% in Area-3.
Operating condition 3	Increased power rating of IBR1 and IBR2 from 250 MW to 350 MW; Increased power rating of WTS from 250 MW to 350 MW.
Operating condition 4	Add transmission line between buses 5-6 and buses 5-12; Decrease the WTS power rating of 250 MW to 150MW; Decrease IBR1 power rating of 250 MW to 150 MW.

The damping performance of the proposed SDC for IBRs in system LFO modes under different operating conditions is shown in Table 6.5. Further, this work compared the proposed SDC scheme with the SDC design scheme for multiple VSGs presented in [30]. Table 6.5 shows that the damping performance of the proposed SDC in system LFO modes is better than the SDC scheme [30] under different system operating conditions. Although the damping ratio of system LFO modes slightly decreases as the operating conditions change from the normal operating condition, it is still greater than 12% when the SDC scheme is linked with the IBRs. On the other hand, the SDC scheme suggested in [30] is incapable of providing sufficient damping to LFO modes under changes in system operating conditions. Thus, the proposed SDC provides sufficient damping to mitigate system LFO and improve system oscillation performance.

Table 6.5: Damping performance study system with proposed SDC for IBRs under different operating conditions

Operating conditions	Control scheme	Damping ratio (%) of LFO modes					
		$\lambda_{1,2}$	$\lambda_{3,4}$	$\lambda_{5,6}$	$\lambda_{7,8}$	$\lambda_{9,10}$	$\lambda_{11,12}$
OC-1	SDC [30]	9.59	10.31	10.35	11.49	11.18	11.22
	Proposed SDC	13.90	13.71	17.13	16.32	14.18	17.49
OC-2	SDC[30]	9.17	10.48	9.61	10.48	9.98	9.59
	Proposed SDC	13.48	13.0	15.64	16.18	15.01	16.50
OC-3	SDC[30]	8.79	9.65	8.56	9.91	9.38	9.54
	Proposed SDC	11.26	12.08	15.50	17.06	14.35	15.61
OC-4	SDC [30]	9.42	9.78	10.05	10.62	9.19	8.99
	Proposed SDC	13.43	13.71	15.93	16.62	15.52	16.84

6.6.2 Dynamic simulation analysis on RTDS

In this simulation, the IEEE 39 system and the proposed SDC for IBRs are modelled in the RSCAD FX 2.2 draft using the mainstep interface with a time constant of 50 μs, while the IBRs are modelled in the RSCAD FX 2.2 draft using the substep interface with a time constant of $5\mu s$. The dynamic simulation analysis is performed under different operating conditions, as mentioned in Table 6.4, with each simulation case considering a 150 ms communication time delay in the wide-area feedback signal for the multi-stage mixed H_2/H_∞ control scheme for the active control loop of each IBR. The study system is simulated under various operating conditions and disturbances, which are described as follows:

6.6.2.1 Dynamic simulation case-1

In this simulation case, the study system operates under normal conditions, with a 3-phase fault applied at the terminal of SG6 at bus 35 at time $t = 2.5s$ for $0.1s$. The dynamic simulation response of the study system with the proposed SDC for each IBRs is shown

in Fig. 6.11.

The power flow through the inter-area line P_{1-39} and the rotor speed difference between SG5 and SG9 (i.e., $\omega_5 - \omega_9$) are shown in Fig. 6.11(a) and (b), respectively. The simulation results demonstrate that the proposed SDC effectively damps power oscillations through the inter-area line and rotor speed oscillations of SGs after the disturbance is applied. The active power output of IBR1 (P_{p1}) is shown in Fig. 6.11(c), indicating that the power oscillation of IBR control via VSG technique with associated SDC control is significantly reduced. Additionally, the simulation responses of DC-link voltage (V_{cd1}) for IBR1 are depicted in Fig. 6.11(d). These results demonstrate that the oscillation magnitude is effectively damped, and the settling time is considerably reduced with the proposed SDC for IBRs. Thus, the dynamic simulation response confirms that the proposed SDC for IBRs provides superior damping to mitigate system oscillations compared to the PSS-based SDC suggested in [30] for the reactive control loop of VSG control.

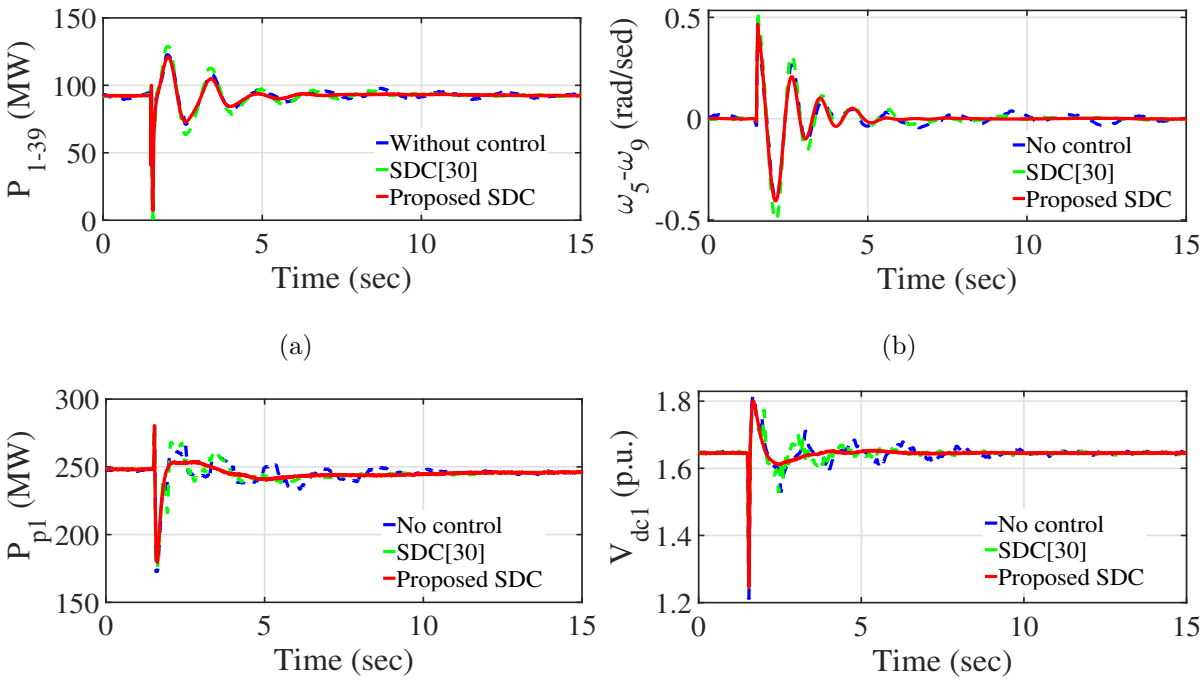

Figure 6.11: The dynamic response of New England 39-bus system with IBR operating under operating condition-1. (a) P_{1-39}, (b) $\omega_5 - \omega_9$, (c) P_{p1}, and (d) V_{cd1}.

6.6.2.2 Dynamic simulation case-2

The study system is simulated under operating condition-2, as described in Table 6.4. A 3-phase fault is applied to the transmission line between buses 25 and 26 at $t = 2.5s$ for a duration of $0.1s$.

The dynamic response of power flow in the inter-area tie line P_{1-39} is depicted in Fig. 6.12(a). The proposed SDC for IBR significantly reduces peak overshoot and settling time in inter-area line power oscillations compared to the existing PSS-based SDC [30]. Fig. 6.12(b) illustrate the dynamic simulation response of the rotor speed difference between the dominant SGs in the study system, specifically SG2-SG10 (i.e., $\omega_2 - \omega_{10}$), which participate in system LFO modes. These responses show that the rotor oscillations of the dominant SGs are effectively damped. Fig. 6.12(c) and (d) show the active power of IBR1 and the rotor speed of the induction generator (ω_r) in the wind turbine system. The proposed SDC for IBR provides sufficient damping to mitigate the power oscillation of IBR associated with the VSG technique and the rotor speed oscillation of the induction generator. These results confirm that the proposed SDC enhances system stability by improving damping performance and reducing oscillations.

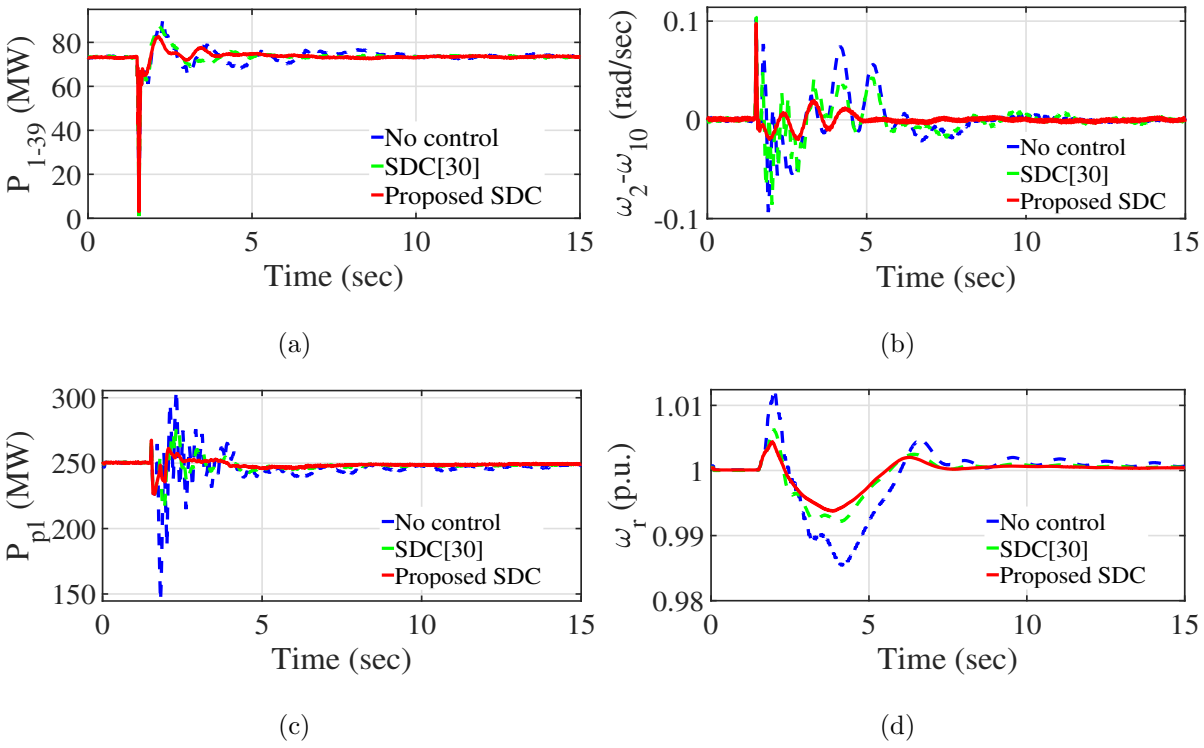

Figure 6.12: The dynamic response of New England 39-bus system with IBR operating under operating condition-2. (a) P_{1-39}, (b) $\omega_2 - \omega_{10}$, (c) P_{p1}, and (d) ω_r.

6.6.2.3 Dynamic simulation case-3

A 3-phase fault is triggered at the PCC of IBR1 at $t = 2.5s$, lasting for $0.1s$. This simulation case simulates the study system under operating condition-3, as mentioned in Table 6.4.

The dynamic simulation response of power flow through inter-area line P_{3-18} and the active power output of IBR1 are shown in Fig. 6.13(a) and (b), respectively. These simulation results indicate that the proposed SDC for IBR provides adequate damping to suppress power oscillations in both the inter-area line and IBR1 after a disturbance. Fig. 6.13(c) and (d) illustrate the rotor speed difference between SG5 and SG9, as well as the frequency response of SG2 (i.e., f_{G2}). These responses show effective suppression of rotor and frequency oscillations of the dominant generators participating in system LFO under operating condition 3. These simulation responses reveal that the proposed SDC for IBR significantly suppresses system oscillations and enhances damping performance more efficiently compared to the existing SDC suggested in [30].

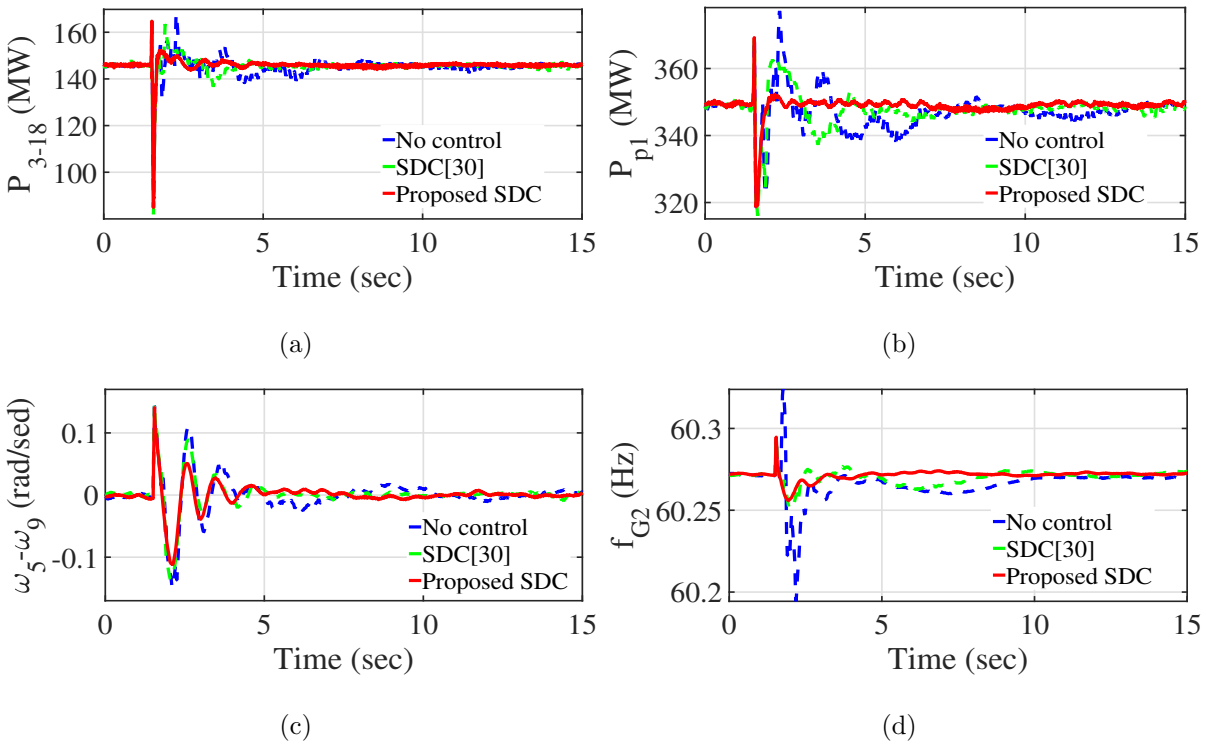

Figure 6.13: The dynamic response of New England 39-bus system with IBR operating under operating condition-3. (a) P_{3-18}, (b) P_{p1}, (c) $\omega_5 - \omega_9$, and (d) f_{G2}.

6.6.2.4 Dynamic simulation case-4

This simulation case studies the system under operating condition-4 as described in Table 6.4, with a 3-phase fault applied on the transmission line between buses 5 and 8 at $t = 2.5s$ for $0.1s$. In this scenario, transmission lines between buses 5 and 6 and between buses 5 and 12 are added. The line parameters for these added transmission lines are identical to those of the transmission line between buses 5 and 8 in the study system.

The power flow through the transmission line P_{5-12} and the output active power of IBR1 are depicted in Fig. 6.14(a) and (b), respectively. The proposed SDC for IBR effectively reduces power oscillations in the transmission line and IBR1 after the disturbance. Further, the dynamic simulation responses of the dominant SGs rotor speed deviation, specifically SG5-SG9 and SG6-SG3 (i.e., $\omega_6 - \omega_3$), are shown in Fig. 6.14(c) and (d), respectively. These responses demonstrate that the proposed SDC provides adequate damping to mitigate system oscillations efficiently, reducing peak overshoot and settling time. The damping performance of the proposed SDC for IBR is superior to that of the SDC suggested in [30].

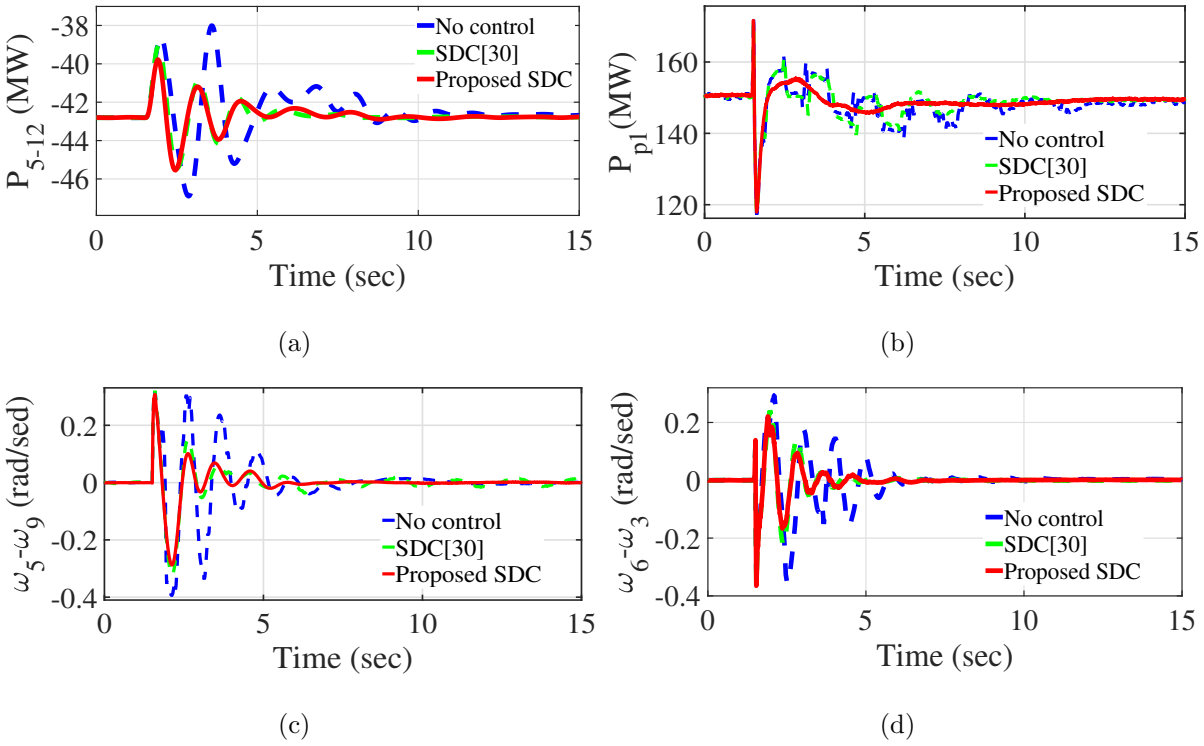

Figure 6.14: The dynamic response of New England 39-bus system with IBR operating under operating condition-4. (a) P_{5-12}, (b) P_{p1}, (c) $\omega_5 - \omega_9$, and (d) $\omega_6 - \omega_3$.

Dynamic simulation results indicate that the proposed SDC for IBRs delivers robust

damping performance across different conditions, including network topology changes, system loading variations, and wind power fluctuations. It also performs well despite uncertainties like VSG voltage loop perturbations and communication delays.

6.7 Summary

This chapter investigates the impact of integrating IBRs controlled via the VSG technique into a low-inertia bus of a multi-machine power system on system LFO damping performance. Simulation results show that the dynamic interaction between VSG-controlled IBRs and the power network introduces new oscillation modes, affecting LFO damping, whereas grid-following IBR control does not introduce new modes. Eigenvalue analysis reveals that increasing the inertia constant of the IBR's active control loop reduces damping performance and increases LFO frequency, while increasing the damping coefficient enhances damping and decreases LFO frequency. Furthermore, the ω, θ_r and V^* state variables of VSG-controlled IBRs significantly influence LFO modes and damping. It was observed from the simulation results that the proposed SDC scheme significantly improves the damping performance of system LFOs as well as effectively mitigates the power oscillations of IBRs under various operating conditions.